Journal of Power Sources 206 (2012) 301–309

Contents lists available at SciVerse ScienceDirect

Journal of Power Sources

journal homepage: www.elsevier.com/locate/jpowsour

Short communication

Percolating networks of TiO_2 nanorods and carbon for high power lithium insertion electrodes

Dominic Bresser[a], Elie Paillard[a,*], Enrico Binetti[b], Steffen Krueger[a], Marinella Striccoli[c], Martin Winter[a], Stefano Passerini[a,**]

[a] Institute of Physical Chemistry, University of Muenster, Corrensstr. 28/30, 48149 Muenster, Germany
[b] Department of Chemistry, University of Bari, Via Orabona 4, I-70126 Bari, Italy
[c] CNR-IPCF Division of Bari, Via Orabona 4, I-70126 Bari, Italy

ARTICLE INFO

Article history:
Received 10 November 2011
Accepted 26 December 2011
Available online 31 January 2012

Keywords:
TiO_2
Anatase
Nanorods
Lithium-ion anode
Battery

ABSTRACT

Anatase TiO_2 nanorods (NRs), with an average diameter of 3–4 nm and an average length of 25–30 nm were investigated as Li-insertion material. The NRs, capped with oleic acid, were synthesized by a low temperature colloidal route based on thermal decomposition of the precursors in presence of coordinating agents. A highly porous and connective network of NRs and carbon was prepared by taking advantage of this organic capping to inhibit the nanoparticle agglomeration and to act as a precursor for the formation of a carbonaceous percolating network. Composite electrodes, made of such material, were able to deliver reversible capacities of about 250 mAh g^{-1} (corresponding to 0.75 equiv. of Li per TiO_2 unit). Reversible capacities of 210 mAh g^{-1} (0.63 Li per TiO_2), 194 mAh g^{-1} (0.58 Li per TiO_2), 165 mAh g^{-1} (0.49 Li per TiO_2), and 130 mAh g^{-1} (0.39 Li per TiO_2) were observed during cycle tests at 1C, 2C, 5C, and 10C, respectively, confirming the excellent high rate performance of the well-dispersed NRs. Finally, the electrodes showed excellent cycle life performance.

1. Introduction

The interest in renewable energy sources is nowadays more relevant than ever. Beside concerns about the climate change as well as decreasing resources of coal, gas, and oil, the harrowing nuclear crisis in Japan has, last but not least, marked a watershed for an increasing demand for green, safe, and renewable energy sources. This increasing demand and the concurrent change of mind in wide sections of the population about energy resources has and will have a deep impact towards research in renewable energy systems and adjacent research fields. According to Jacobson and Delucchi [1,2] it appears to be possible to provide at least considerable amounts of global energy demand by solar, wind, and water power plants by 2030. But these technologies, particularly wind and solar power, entail one major drawback, which is the intermittency of its energy supply, being strongly dependent on the current meteorological conditions. Thus miscellaneous systems for storing energy are discussed and investigated, among them storage technologies for hydrogen, methanol, or hydrocarbon [3].

However, with respect to progressive solutions for energy storage, e.g., by plug-in hybrid electric vehicles and vehicle-to-grid concept [4], which offer a solution to one of the major future issues, providing energy for transportation, electrochemical energy storage devices occur to be one of the most promising technologies for efficient energy storage [5].

Due to their high energy density, long cycle life, and efficient energy storage, lithium ion batteries are currently being considered as the leading candidate to meet the demands of electrochemical energy storage for hybrid and electric vehicles and renewable energy sources. However, the upscaling of the present chemistry, which is based on $LiCoO_2$ and graphite, will certainly raise issues on materials availability, costs, and safety [6,7]. Focusing on the anode side, graphite and carbonaceous materials entail several disadvantages, especially in terms of safety, poor rate capability, and irreversible capacity loss in the first cycle, the latter being due to the initial decomposition of the electrolyte and formation of the solid electrolyte interphase (SEI) [8,9]. This decomposition is caused by the lithium insertion in graphite electrodes taking place at a potential below the electrochemical stability window of the conventional alkyl carbonate based electrolytes presently used [6,9,10].

Thus, there is a special need for safer and most effective anode materials particularly with improved high rate capability. Among others, titanium oxides (TiO_2) have attracted great interest in recent years due to their ability to reversibly insert

* Corresponding author.
** Corresponding author. Tel.: +49 251 8336026; fax: +49 251 8336032.
E-mail addresses: Elie.Paillard@uni-muenster.de (E. Paillard), Stefano.Passerini@uni-muenster.de (S. Passerini).

0378-7753/$ – see front matter © 2011 Elsevier B.V. All rights reserved.
doi:10.1016/j.jpowsour.2011.12.051

considerable amounts of lithium within the electrochemical stability window of common organic electrolytes. Beside this, TiO_2 offers several other advantages as being biocompatible, environmentally friendly, abundant and inexpensive [6]. For example, the higher lithium insertion potential compared to graphite prohibits the risk of electrolyte decomposition and/or metallic lithium deposition in normal operating conditions and upon moderate overcharges [6].

Research in the field of TiO_2 has focused particularly on the polymorphs of rutile and anatase TiO_2, as well as TiO_2-B. The first studies on micrometer-sized TiO_2 polymorphs showed reasonable amounts of reversibly inserted lithium only for the anatase materials. However, although the theoretical capacity for lithium insertion in TiO_2 is 335 mAh g^{-1} (corresponding to 1 Li per TiO_2 unit; this ratio is hereinafter expressed as *x.xx* Li/TiO_2), practically, only around 0.5 Li could be reversibly inserted, corresponding to only 168 mAh g^{-1} [11–13].

Following the general tendency of downsizing, and by this taking advantage of typically shorter diffusion lengths for electrons and Li^+ ions, decreased current density per unit surface area, higher electrode–electrolyte contact area, better strain accommodation during lithium insertion/extraction [7,14,15], and extended solid solution domains [16,17], the use of TiO_2 polymorph nanoparticles led to improved results in terms of high rate capability, rate and cycling stabilities as well as higher capacities [16–19]. In particular, nanometer-sized particles with a one-dimensional (1D) structure, such as nanotubes, nanorods, and nanowires, have attracted great interest due to easy Li^+ ion diffusion into the TiO_2 host structure caused by their high specific surface area [20] and low particle size [21]. For nano-sized rutile TiO_2, Pfanzelt et al. [22] recently reported a reversible capacity of about 315 mAh g^{-1} (0.94 Li/TiO_2) within the potential window extending from 0.1 V to 3.0 V. However, the authors also reported some important drawbacks such as the high irreversible capacity in the first cycle (≈310 mAh g^{-1}), the fast decay of the observed capacity especially for elevated charge/discharge rates, and, finally, the electrode operation beyond the electrochemical stability window of common electrolytes. TiO_2-B nanowires, studied by Armstrong et al. [23], presented a rather interesting reversible capacity of around 200 mAh g^{-1} (0.60 Li/TiO_2) for an applied current density of 200 mA g^{-1}.

Most of the studies, however, focused on the electrochemical investigation of nano-sized anatase TiO_2 because micro-sized particles of such a material seemed for several years to be the only polymorph allowing the insertion of significant amounts of lithium. The electrochemical performance of anatase nanotubes was reported, inter alia, by Xu et al. [20], showing a maximum reversible capacity of 238 mAh g^{-1} (0.71 Li/TiO_2) in the first cycle, which decayed to 198 mAh g^{-1} (0.59 Li/TiO_2) at the 20th cycle. At higher current densities, however, the observed reversible capacities were substantially lower (171 mAh g^{-1} (0.51 Li/TiO_2) at 140 mA g^{-1} and 168 mAh g^{-1} (0.5 Li/TiO_2) at 210 mA g^{-1}). Higher reversible capacities (248 mAh g^{-1} or 0.74 Li/TiO_2 in the first cycle) and stable cycling performance at elevated charge/discharge rates were reported by Li et al. [24].

The electrochemical investigation of anatase TiO_2 nanorods was, among others, reported by Gao et al. [21] and Bao et al. [14] with reversible capacities of around 190 mAh g^{-1} (0.57 Li/TiO_2) in the first cycle. Nanorods offer, in general, one main advantage compared to nanotubes. They show a typical two-phase equilibrium flat plateau during charge and discharge, which nanotubes do not show normally [24,25]. Thus nanorods present the advantage of a constant potential for varying amounts of inserted/extracted lithium, which is preferable for the application as anode in lithium ion batteries [26].

In this work, oleic acid (OLEA) capped anatase TiO_2 nanorods (NRs) were synthesized by an airless low-temperature colloidal chemistry process, providing the feasibility of separating nucleation from growth, inhibiting the formation of secondary particles by agglomeration and controlling particle growth in terms of size and geometry [27].

However, the application of these well dispersed NRs as electrode material strongly necessitates new approaches for the electrode preparation process, since the Super P particles with an average diameter of 35–40 nm are not sufficiently small for ensuring the required overall connecting conductive network as they do for micro-sized particles (Fig. 1, path B). Thus, additional conductive pathways are sorely needed, inhibiting simultaneously particle agglomeration and by this preserving the advantages resulting from the synthesis of well dispersed nanoparticles leading to the outstanding electrochemical performances accruing from the use of nanomaterials in general as already mentioned.

Consequently, for the electrode preparation we used a new, in-house developed technique (Fig. 1, path A), which takes advantage of the organic capping as dispersing agent to avoid particle agglomeration while preparing first a TiO_2-NRs–Super P composite by mixing the soluble organic capped NRs with Super P, and upon further calcination as conductive agent, by thermally induced conversion into carbon, to contribute to the electron conductive percolating network as schematically shown in the final TiO_2-NRs–carbon composite.

For the electrochemical investigation of the TiO_2-NRs, cyclic voltammetry and galvanostatic cycling were performed with a special focus on the identification of the operating electrode voltage window in order to optimize the balance between high initial capacity and long-term cycling performance. The anatase TiO_2-NRs electrodes showed excellent electrochemical performances in terms of reversible capacity, cycling stability, faradic efficiency, and high rate capability.

2. Experimental

2.1. Synthesis of oleic acid-capped anatase TiO_2-NRs

The synthesis of oleic acid (OLEA) capped anatase TiO_2 nanorods (NRs) was performed by using a standard airless technique [50–53]. In brief, OLEA-capped TiO_2 NRs were synthesized by adding titanium tetraisopropoxide (TTIP) under a nitrogen flow at 100 °C to previously degased technical grade OLEA, which was used as surfactant. The anhydrous environment prevented TTIP from premature hydrolysis. Subsequent injection of an aqueous solution of trimethylamine-*N*-oxide (TMAO) dihydrate started the fast hydrolysis, by which the formation of OLEA-capped anatase TiO_2-NRs was obtained. Characterization of the morphology as well as particle size and shape were carried out by powder X-ray diffraction (XRD) on a Bruker D8 Advance (Cu-Kα radiation, λ = 0.154 nm) and transmission electron microscopy (TEM), which was performed on samples deposited on a carbon-coated 400 mesh copper grid, using a JEOL TEM microscope operating at an accelerating voltage of 100 kV.

2.2. TiO_2–C composite preparation

The obtained anatase TiO_2-NRs, containing 24.5% of organic material (OLEA), as determined by thermogravimetric analysis (TGA) under O_2 (TA Instruments Q5000), were mixed with Super P conductive carbon (TIMCAL) in a 90:10 (TiO_2/C) weight ratio in CH_2Cl_2. The mixture was then homogenized using a planetary ball mill (Vario-Planetary Mill Pulverisette 4, FRITSCH) set at 800 rpm for 3 h. The composite was allowed to dry overnight at RT and was then annealed at 350 °C (in air) for 12 h. TGA and XRD characterizations showed that such a thermal treatment does not result in any weight loss for Super P or phase transformation of the TiO_2-NRs,

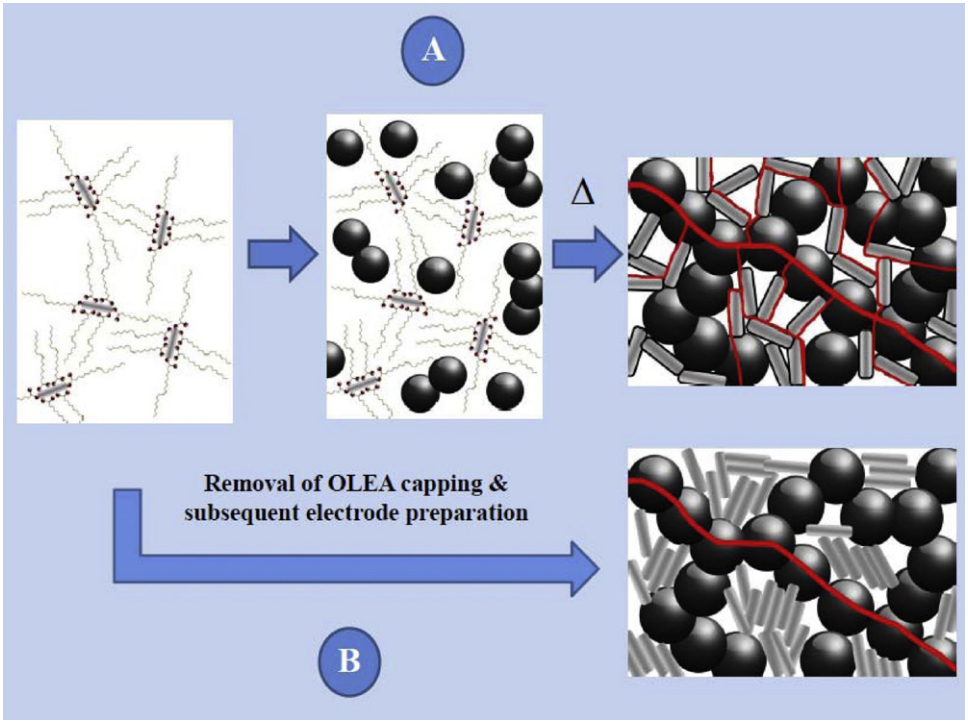

Fig. 1. (A) Schematic drawing of the carbonization process of the OLEA, resulting in the TiO_2-NRs–carbon composite. (B) Alternative process, removing the OLEA capping in a first step before further electrode material preparation. (A) and (B) The red line illustrates possible pathways for electron diffusion. (For interpretation of the references to color in this figure legend, the reader is referred to the web version of the article.)

but allows the carbonization of the OLEA. A TGA performed after this step revealed an 85:15 weight ratio (TiO_2/C) for the composite, showing that some OLEA residue was remaining within the composite, forming a carbonaceous layer on the surface of the TiO_2-NRs, as confirmed by Raman spectroscopy using a SENTERRA Raman spectrometer (BRUKER Optics), equipped with a 532 nm laser and an output power of 2 mW. The preservation of single-phase anatase crystal structure of the TiO_2-NRs was confirmed by XRD analysis, using a Bruker D8 Advance (Cu-Kα radiation, $\lambda = 0.154$ nm).

2.3. Preparation of TiO_2-NRs electrodes

The TiO_2-NR/C composite material was mixed with PVDF-HFP copolymer (Kynarflex 2801, ARKEMA), as the binder, in an 88:12 weight ratio. No additional carbon was used for the electrode preparation. N-methylpyrrolidinone (ALDRICH) was used as the solvent. The dry composition of the slurry was 75 wt%. TiO_2-NRs, 13 wt.% carbon and 12 wt.% PVDF-HFP. The slurry was homogenized using planetary ball milling at 800 rpm for 1 h (Vario-Planetary Mill Pulverisette 4, FRITSCH). The resulting slurry was then casted on dendritic copper foil (SCHLENK) by using a laboratory doctor blade, with a wet film thickness of 120 μm. The electrodes were dried in air for 1 h at 80 °C then 12 h at RT. Disk electrodes (12 mm diameter) were then punched and dried for 12 h at 120 °C under vacuum. The active material mass loading was comprised between 1.5 and 1.7 mg cm^{-2}.

2.4. Electrochemical characterization

Electrochemical studies were carried out in three-electrode Swagelok™-type cells, with lithium metal foils (CHEMETALL, lithium battery grade) used as counter and reference electrodes. The cells were assembled in an MBraun glove box with oxygen and water contents below 0.5 ppm. A stack of polypropylene fleeces (Freudenberg FS 2226) drenched with a 1 M solution of $LiPF_6$ in a 3:7 volume mixture of ethylene carbonate and diethyl carbonate (UBE) was used as the electrolyte. Since lithium foil was used as counter and reference electrode, all the potential values given in this manuscript refer to the Li^+/Li reference couple.

All electrochemical studies were performed at 20 ± 1 °C. For galvanostatic cycling, a Maccor Battery Tester 4300 was used. Cyclic voltammetry experiments were performed by mean of a Solartron 1287 potentiostat and a VMP3 potentiostat (BioLogic). Galvanostatic cycling and cyclic voltammetry were performed in three different potential ranges ranging from 3.0 V (cathodic limit) and either 0.1, 1.0 or 1.2 V (anodic limit). For the galvanostatic measurements a charge/discharge rate of 1C corresponds to a current density of 168 mA g^{-1}, considering $x = 0.5$ as the reference limit of the insertion reaction: $TiO_2 + x(Li^+ + e^-) \rightarrow Li_xTiO_2$. For the cyclic voltammetry a scan rate of 0.05 mV s^{-1} was applied.

Ex situ, high resolution scanning electron microscope (HRSEM) analysis was carried out on a ZEISS Auriga® microscope on pristine and cycled (50 cycles with 1.0 V as the lower cut-off potential) electrode.

3. Results and discussion

3.1. Morphological and structural characterization

The as-prepared TiO_2-NRs shape and size was determined by TEM analysis. From Fig. 2, it can be clearly seen that the single particles are well separated due to the OLEA capping agent. The NRs are in average 3–4 nm in diameter and 25–30 nm in length.

XRD analysis was performed before and after the carbonization of the OLEA capping (Fig. 3). The resulting pattern of the OLEA capped NRs can be mainly indexed as belonging to the anatase phase (ICSD 172914) with the $I4_1/amd$ space group. But there are three additional peaks of very low intensity, related to phase impurities (marked by *). Unfortunately, without further crystallographic investigation, these peaks cannot definitely be assigned to

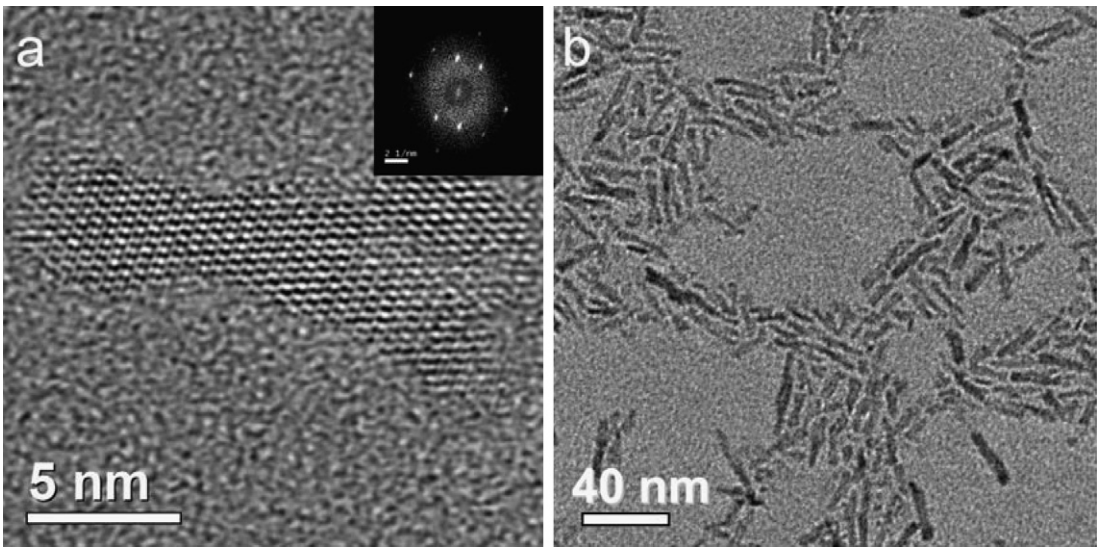

Fig. 2. TEM images of the as-prepared anatase TiO_2-NRs with different magnifications. Inset, the corresponding Fourier transform.

a certain phase. Thus, it can just be assumed that these peaks are related to a very minor amount of brookite TiO_2, since it is already reported as possible phase impurity [28,29] and the 2θ positions of the observed peaks match rather well [29,30].

However, these additional peaks disappear during the thermal treatment and phase pure anatase TiO_2-NRs are obtained (Fig. 3b). Thus it is ascertained, that no phase change from anatase to rutile appeared during this process. Although it is known that the rutile phase is the thermodynamically favored one for TiO_2 [31,32], the temperature dependency of the phase transformation from anatase to rutile is strongly influenced by the particle size. As reported by Chen et al. [33], anatase TiO_2-NRs (4 nm in diameter and 35 nm in length), synthesized by the same method as described above, did not undergo any phase transformation to the thermodynamically favored rutile phase up to 850 °C. This enhanced phase stability is likely caused by the lower surface free energy of the anatase phase as compared to the rutile phase, whose influence on the total free energy increases with decreasing particle size and thus increasing surface area [31,32,34].

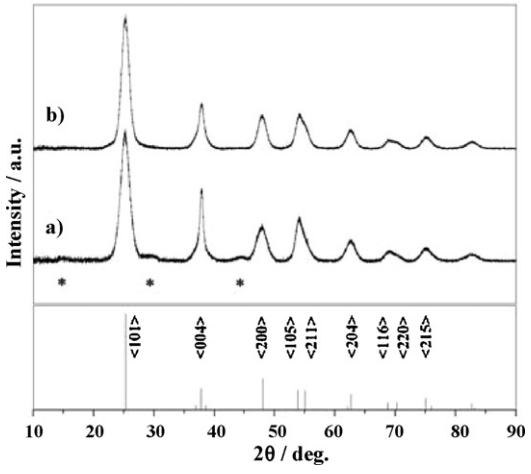

Fig. 3. XRD pattern of the oleic acid capped TiO_2-NRs before the carbonization step (a) and the composite material (TiO_2-NRs/C) after thermal treatment at 350 °C in air (b). The anatase TiO_2 reference ICSD 172914 is shown in the bottom. Additional peaks for (a) are marked by *, corresponding to brookite TiO_2.

Finally, the characteristic line broadening of the diffraction peaks (Fig. 3a), which is maintained upon the thermal treatment (Fig. 3b), indicates the nanocrystallinity of the TiO_2-NRs and confirms its preservation. Moreover, we observe a higher and narrower ⟨0 0 4⟩ diffraction peak comparatively to XRD patterns of spherical anatase particles [35], confirming the rodlike morphology with a preferred growth orientation along the ⟨0 0 4⟩ direction of the anatase lattice.

For further analysis of the carbon remaining in the TiO_2-NRs–carbon composite, Raman spectroscopy was performed (Fig. 4). The Raman spectra of the oleic acid capped TiO_2 nanorods (before the carbonization step) and the TiO_2-NRs–carbon composite (after the carbonization step) are shown in Fig. 4a–e.

In Fig. 4a the typical vibrations for oleic acid in the high-wavenumber region can be observed for the nanorods sample before the carbonization step with the characteristic three Raman bands between 1050 and 1500 cm^{-1} [36]. However, these bands disappear after the carbonization step and the two characteristic bands for carbonaceous materials occur (Fig. 4b), namely the G-band at around 1580 cm^{-1} for graphitic C–C stretching and the D-band for induced disorder at around 1350 cm^{-1}. The little shoulder at lower wavenumbers around 1100 cm^{-1} corresponds to the vibration of sp^3 hybridized carbon [37,38]. Comparing this spectrum with the Raman spectrum for Super P only, which has been thermally treated in the same way and only shows the characteristic G- and D-band, indicates the formation of an amorphous carbonaceous layer on the surface of the TiO_2-NRs by the residual carbonized oleic acid comprised within the sample.

However, it appears worth mentioning, that the Raman spectrum of Super P changes during the thermal treatment, as the vibration of sp^3 hybridized carbon disappears and the intensity of the G- and D-band increase, suggesting an enhanced electronic conductivity of the Super P due to an increased sp^2 hybridization of the carbon atoms (Fig. 4c).

The formation of a carbonaceous layer on the NRs surface is confirmed by the comparison of the low-wavenumber regions for the two samples in Fig. 4d. The observed bands for the oleic acid capped sample match very well the already reported results for anatase TiO_2 [39], while the spectrum of the carbon coated sample does not show any bands at first view. But, by zooming in the spectrum by a factor of 160 (Fig. 4e), the same bands as for the oleic acid capped sample can be observed, although much less intense compared to the spectrum before the carbonization step. The occurrence of these

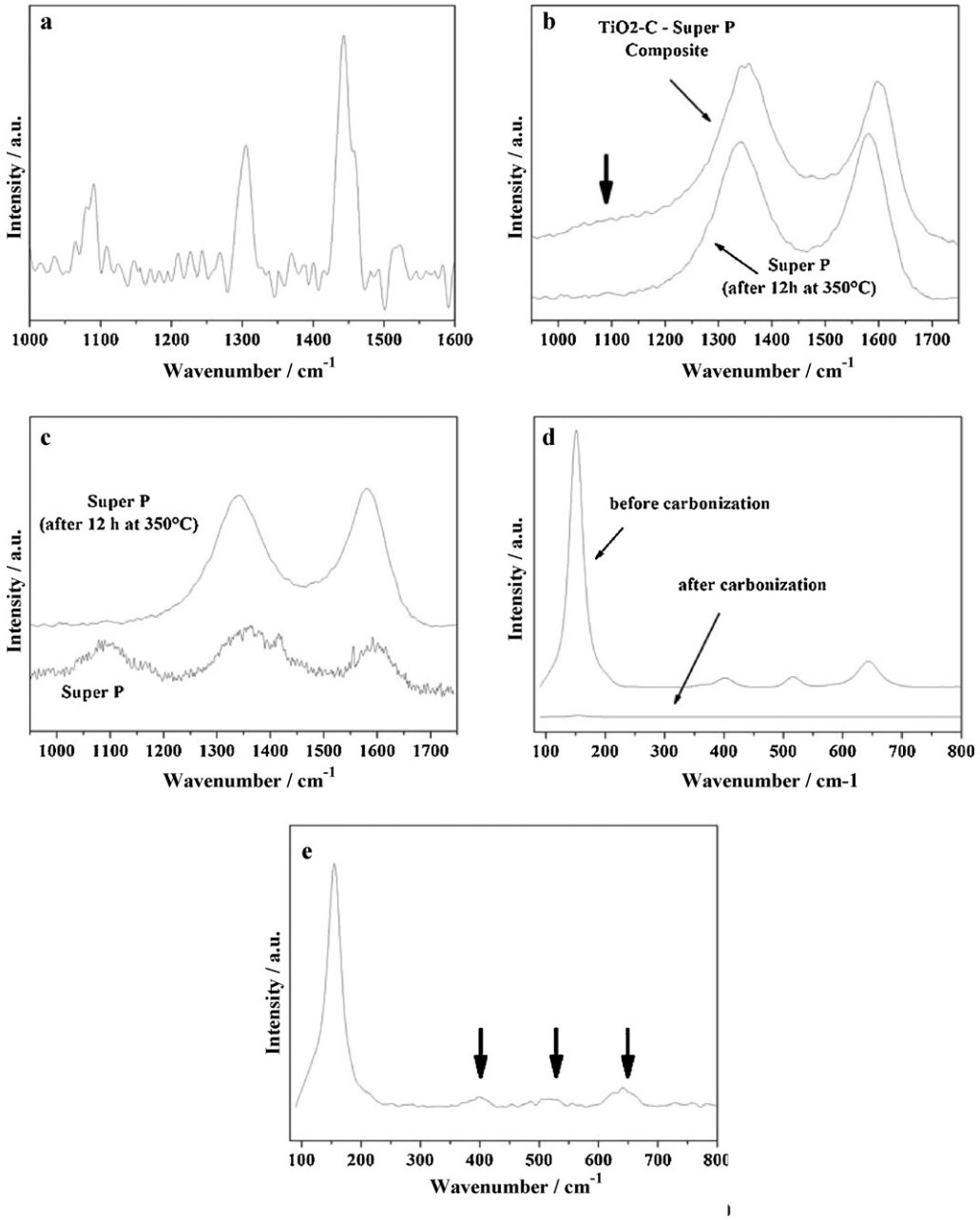

Fig. 4. Raman spectra of the OLEA capped TiO_2-NRs before and the TiO_2-NRs–carbon composite after carbonization. (a) The high-wavenumber region for the OLEA capped TiO_2-NRs. (b) The high-wavenumber region for the thermal treated TiO_2-NRs, including a Raman spectrum of thermally treated Super P only. (c) Comparison of pristine and thermally treated Super P. (d) The low-wavenumber region for the NRs before and after the carbonization step. (e) Magnification of the low-wavenumber region for the TiO_2-NRs–carbon composite by a factor of 160.

bands despite the carbon layer on the particles surface, even if less intense, might be caused by the photocatalytic properties of nano-sized anatase TiO_2 [40–42]. Due to this, the carbon surface tends to decompose during the measurement, due to the light induced photocatalytic oxidation of the carbonaceous layer on the particles surface, caused by the strong oxidizing power of photogenerated holes on the TiO_2 particles surface, leading to the decomposition of organic compounds adsorbed on the particles surface under oxygen atmosphere by release of CO_2 [40–42].

3.2. Cyclic voltammetry experiments

Cyclic voltammetry was carried out with different cathodic potential limits, namely 0.1, 1.0 and 1.2 V. The anodic limit was always set to 3.0 V. The recorded voltammograms during the initial 5 cycles are shown in Fig. 5a–c. All three figures show the characteristic couple of cathodic and anodic peaks at about 1.7 V and 2.0 V, respectively, which agrees well with previously reported values [11–13]. For micrometer-sized anatase TiO_2 only this peak couple is observed, which corresponds to the Li insertion/extraction processes into the TiO_2 host structure [11–13]. During lithium insertion, anatase TiO_2 undergoes a separation in two phases, the Li-poor $Li_{0.01}TiO_2$ phase (space group $I4_1/amd$) with maintained anatase structure and tetragonal symmetry, and the Li-rich $Li_{0.55}TiO_2$ phase (space group *Imma*) with lithium titanate structure and orthorhombic symmetry [17,43,44]. These two phases coexist up to a Li mol fraction of 0.55.

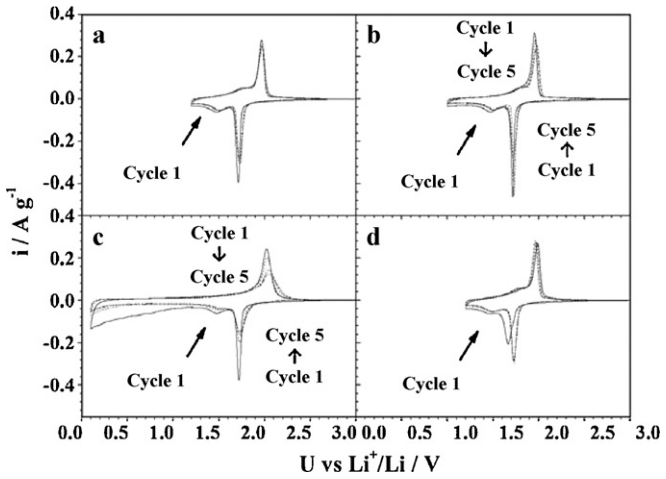

Fig. 5. Voltammograms of a TiO_2-NRs electrode. Scan rate 0.05 mV s^{-1}. Cycle 1–5. (a) Between 3.0 V and 1.2 V. (b) Between 3.0 V and 1.0 V. (c) Between 3.0 V and 0.1 V. (d) Between 3.0 V and 1.2 V. Only 1 day rest after assembling.

In nanometer-sized particles, a second phase transformation ($Li_{0.55}TiO_2 \rightarrow LiTiO_2$) takes place during lithium insertion, leading to anatase $LiTiO_2$ (space group: $I4_1/amd$) [16]. The appearance of this new phase is confirmed by the peak couple seen in Fig. 5a and b at 1.45 V and 1.8 V, respectively for the lithium insertion and extraction processes. This peak couple is never observed in micro-sized particles because the growth of this new occurring phase is limited to a thickness of only about 4 nm, independent of the particle size of the active material particles [16]. Because of this limited growth, the theoretical maximum capacity, corresponding to the complete formation of $LiTiO_2$, can only be achieved with particles smaller than 10 nm in diameter [16,45]. For larger particles, the fully lithiated phase would be present only at the particles surface, while the particle core maintains the $Li_{0.55}TiO_2$ structure. Nevertheless, it is important to notice that the formation of the anatase $LiTiO_2$ phase is suggested to be kinetically limited only at room temperature since a complete phase transformation can be achieved at elevated temperatures even for larger particles [11,16,45].

An additional interesting effect observed with TiO_2-NRs electrodes is the spontaneous change in their CV response depending on the initial rest time. Assembled cells left in rest condition for one day (see Fig. 5d) showed the main peak during the first cathodic scan at a lower potential (1.6 V vs 1.7 V) than those left in rest conditions for longer periods (up to 10 days in Fig. 5a–c). This effect substantially complicated the understanding of the system because of the somehow random appearance of the first cathodic peak between 1.7 V and 1.6 V. However, we also observed that, during the rest period, the cell OCVs spontaneously dropped from an initial value of 3.2–2.7 V after ten days. From a galvanostatic titration on a freshly made cell, this OCV drop was found to correspond to the formation of $Li_{0.03}TiO_2$. The reason of such a spontaneous lithiation is not clear, however, it is reasonable to propose that it originates from a surface reaction with the electrolyte, which could be strongly enhanced by the very high surface area of the TiO_2-NRs. Nevertheless, this spontaneous although very minor lithiation results in a decreased overpotential for lithium insertion, which is comparable to the effect of a full insertion/deinsertion cycle. Van de Krol et al. [46] reported that some lithium ions are irreversibly trapped in the regions where the phase transformation from the anatase Li-poor phase to the titanate $Li_{0.55}TiO_2$ phase takes place, leading to increased conductivity of the material and facilitated lithium insertion.

During the first scan, the behavior of the TiO_2-NR electrodes appears to be strongly affected by the cathodic potential limit. For a reversing cathodic voltage limit of 0.1 V (see Fig. 5c) a much larger irreversibility is observed. A large background current is observed below 1.2 V without any corresponding anodic feature. In addition, both the cathodic and anodic peaks sharply decrease during the following cycles. This behavior is clearly explained by an extensive electrolyte decomposition favored by the large surface area of the NRs, leading to the formation of the SEI layer. As a matter of fact, electrolyte decomposition is already observed during the voltammetric test performed with a cathodic limit of 1.0 V as confirmed by HRSEM analysis of a pristine and a cycled electrode (Fig. 6). The comparison of these two HRSEM images clearly shows that a SEI film exists on the cycled electrode although the electrolyte decomposition is usually not reported to take place at these potentials. However, this might be caused by the electrocatalytic properties of TiO_2, as already reported in literature [47,48].

3.3. Galvanostatic tests

To evaluate the charge/discharge performance of the TiO_2-NR electrodes, galvanostatic cycling tests have been carried out between 3 V (charge limit) and three different discharge cut-off voltages: 0.1, 1.0 and 1.2 V. The results are shown in Figs. 7–9.

Setting the cut-off potential at 1.2 V (Fig. 7a) and the rate at C/10 resulted in the electrode reversible capacity in the first cycle to be 245 mAh g^{-1}, corresponding to 0.73 Li^+ per TiO_2. An irreversible capacity of about 60 mAh g^{-1} was observed, due to the lithium trapping mechanisms discussed earlier [46]. The delivered capacity at 1C rate was as high as 210 mAh g^{-1} (0.63 Li/TiO_2) with a faradic efficiency higher than 99%. At even higher C rates the electrodes

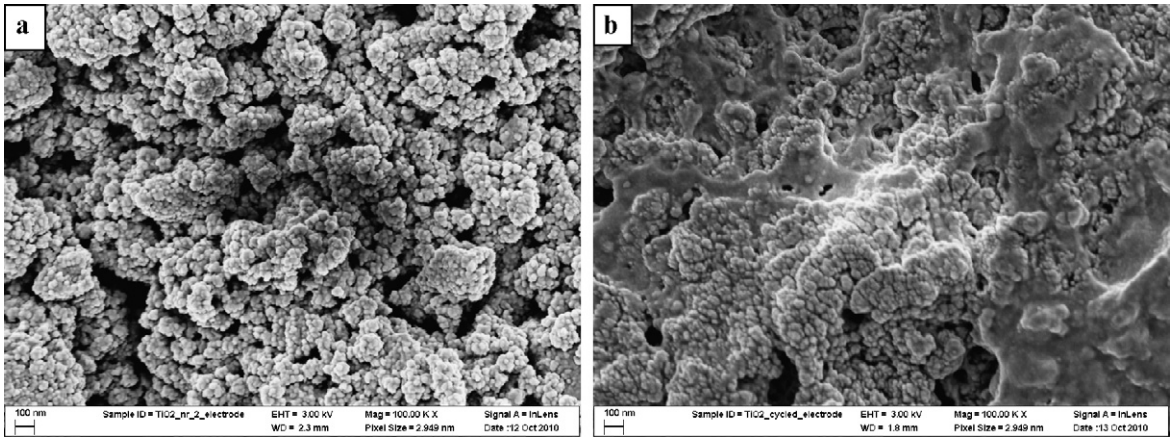

Fig. 6. HRSEM images of aTiO_2-NR electrodes (a) pristine and (b) after 50 cycles. Cut-off voltage: 1.0 V.

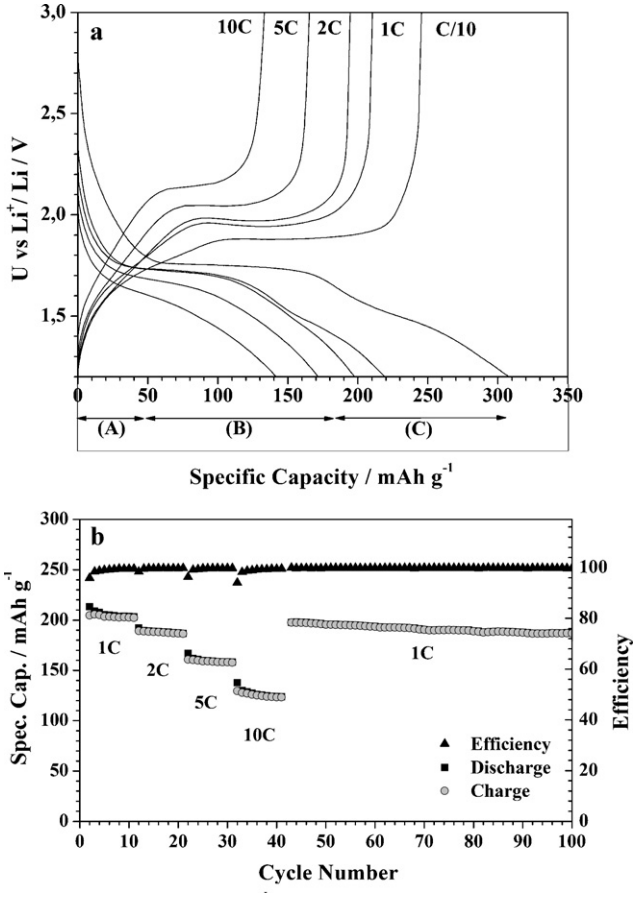

Fig. 7. Galvanostatic charge discharge tests at different C rates. Lower cut-off potential: 1.2 V. (a) Voltage profile vs specific capacity of a TiO_2-NRs electrode. (b) Specific capacity of a TiO_2-NRs electrode. 1st cycle not shown.

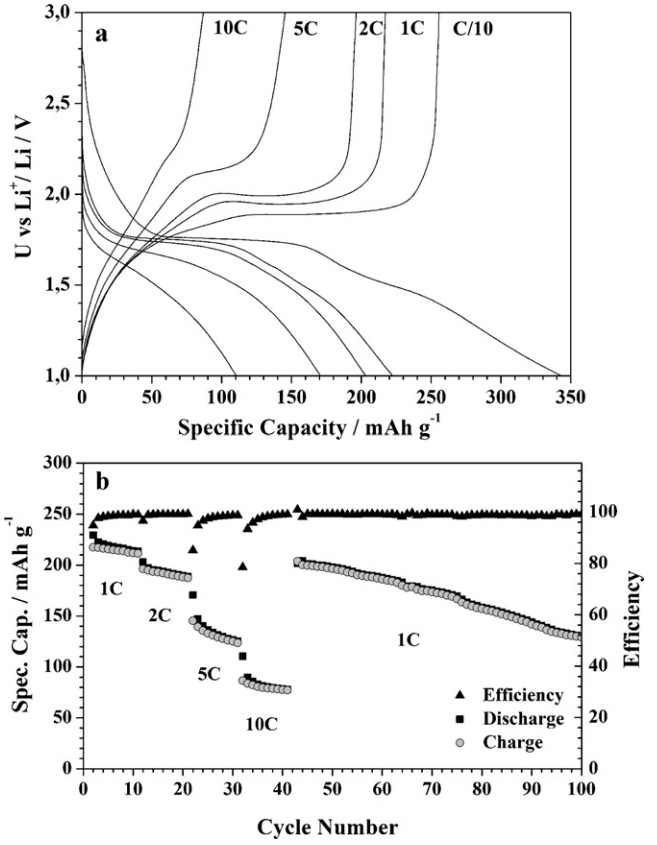

Fig. 8. Galvanostatic charge discharge tests at different C rates. Lower cut-off potential 1.0 V. (a) Voltage profile vs specific capacity of a TiO_2-NRs electrode. (b) Specific capacity of a TiO_2-NRs electrode. 1st cycle not shown.

still delivered high reversible capacities, namely 194 mAh g^{-1} at 2C, 165 mAh g^{-1} at 5C (this capacity corresponds to 0.5 mol of Li^+ per mole of TiO_2) and 130 mAh g^{-1} at 10C, thus demonstrating the high rate capability of the investigated NRs.

While the typical plateau of anatase TiO_2 is always observed, except at the highest rate (10C), a more careful observation of the discharge voltage profile at C/10, reveals the existence of three different regions: (A) from 3.0 V to 1.8 V, corresponding to a capacity of around 50 mAh g^{-1}; (B) the constant voltage plateau extending for about 135 mAh g^{-1}; and (C) below 1.8 V, i.e., after the main voltage plateau, where additional 125 mAh g^{-1} of lithium are inserted.

The capacity observed for region (A) (0.15 mol of Li per mole of TiO_2) agrees with the extended domain of the Li-poor phase solid solution already reported for nanosized TiO_2 particles, which are characterized by a very large fraction of insertion sites close to the particle surface [16,17,49].

In region (B) the typical plateau associated with the Li-poor to Li-rich phase transformation is observed, which capacity corresponds to the formation of $Li_{0.55}TiO_2$. At higher C rates, however, the well-defined constant voltage plateau becomes shorter and turns into a slope at 10C.

Finally, in region (C) the second phase transformation from the Li-rich TiO_2 phase (*Imma*) to the anatase Li_1TiO_2 phase ($I4_1/amd$) takes place. This transformation is reflected in the appearance of a plateau around 1.5 V during the C/10 discharge [49]. At C/10 discharge rate the final composition achieved was $Li_{0.9}TiO_2$, i.e., close to the theoretical lithiation. However, this second phase × transformation ($Imma \rightarrow I4_1/amd$) appears to be strongly affected by the discharge rate increase, as indicated by the sudden disappearance of the plateau in the 2C discharge. The voltage curve of the electrode discharged at 2C overlaps very well that one obtained at 1C rate, except at voltages below 1.5 V, where this plateau would appear. The overall lithium insertion at 2C is limited to $x = 0.58$ (vs 0.66 at 1C), thus suggesting that the second phase change is strongly kinetically limited, particularly for current densities above 1C.

In the corresponding charge profiles (see Fig. 7a) the shortening of the main plateau is also observed as the rate is increased, but, in contrast to the discharge behavior, it is still present even for applied current densities as high as 10C (although its position is shifted to higher voltages upon increasing rates). This behavior indicates lower kinetic limitations for lithium extraction than for lithium insertion.

In Fig. 7b is reported the performance of a TiO_2-NRs electrode subjected to continuous charge/discharge tests at different rates within 3.0 V and 1.2 V cut-off limits. The overall stability of delivered capacity upon cycling at different rates demonstrates the highly stable cyclability of the investigated NRs for a potential range of 1.2–3.0 V. Finally, the high reversibility of the lithium insertion/extraction processes in the TiO_2-NRs electrode after the first cycle is demonstrated by the recovery of the delivered specific capacity when the discharge/charge rate is set back to 1C.

Fig. 8a and b shows the voltage profile and the capacity performance of TiO_2-NR electrodes recorded during the galvanostatic tests at different C rates with the lower cut-off limit of 1.0 V. Although the first cycle reversible capacity is slightly increased with respect to the tests performed using the 1.2 V lower cut-off (255 mAh g^{-1} vs 245 mAh g^{-1} or 0.76 vs 0.73 Li per TiO_2), the cycling performance is, by far, poorer at all C rates. The electrode voltage profiles (Fig. 8a) clearly show that the shortening of the constant

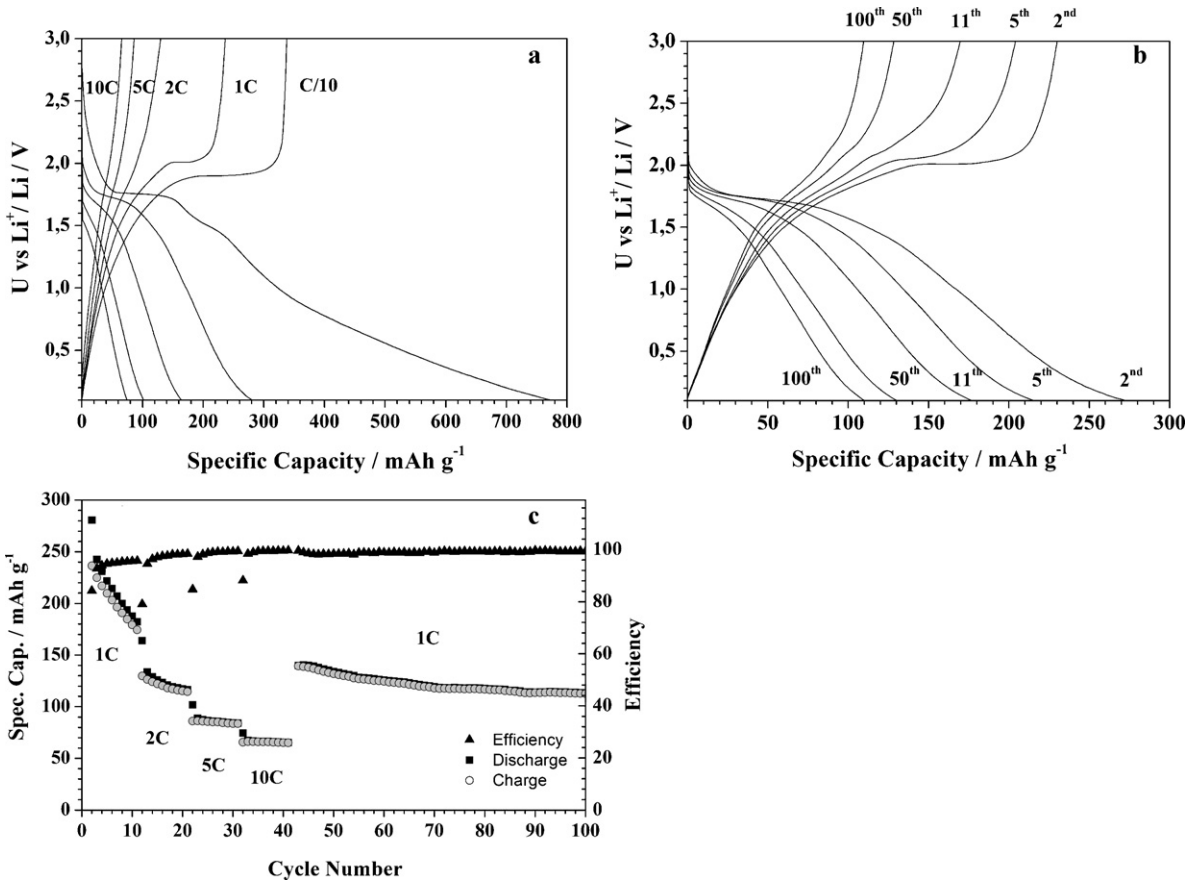

Fig. 9. Galvanostatic charge discharge tests at different C rates. Lower cut-off potential: 0.1 V. (a) Voltage profile vs specific capacity of a TiO_2-NRs electrode. (b) Selected voltage profile vs delivered capacity curves of a TiO_2-NRs electrode subjected to prolonged galvanostatic charge discharge tests. (c) Specific capacity of a TiO_2-NRs electrode. 1st cycle not shown.

voltage plateau for increasing C rates occurred much faster than with the 1.2 V cut-off limit (Fig. 7a). In addition, the first cycle irreversible capacity increases of about 50%, from 60 mAh g^{-1} to about 90 mAh g^{-1}, by lowering the cut off limit from 1.2 V to 1.0 V.

Setting the lower cut-off limit to 0.1 V (see Fig. 9a–c) results in an even more dramatic capacity fading, although, apparently, the reversible capacity in the first cycle was 335 mAh g^{-1}, which corresponds to the full (theoretical) lithiation of TiO_2 and the complete phase transformation to anatase Li_1TiO_2. The irreversible capacity, however, was higher than 430 mAh g^{-1}, thus indicating that several other processes take place in the 1.0 V to 0.1 V interval. The formation of a SEI layer, taking place at the TiO_2-particle surface, has already been mentioned earlier. Eventually, the irreversible formation of covalent-type Li—O bonds [39], caused by applying such strong potential forces, might explain the structural degradation of the material as confirmed by the disappearance of the voltage plateau after only 11 cycles (Fig. 9b). After 100 cycles the material is capable of delivering only 100 mAh g^{-1} (0.3 Li/TiO_2).

To summarize, the galvanostatic cycle tests evidenced 1.2 V as the cut-off limit of choice since the NRs showed the best balance between delivered reversible capacities and cycling stability.

3.4. Power rate tests

The investigation of the electrochemical properties of the NRs for increasing discharge or charge rates were carried out with the cut-off limit set at 1.2 V, as shown in Fig. 10. It can be clearly seen that, as mentioned earlier, lithium insertion is the limiting factor. The capacity decay for elevated charge rates is less pronounced than for elevated discharge rates. These results agree with a former study by van de Krol et al. [46], which indicated that the transport of lithium in the anatase Li-poor phase is faster than in the Li-rich one since the number of unoccupied octahedral sites is higher, thus facilitating lithium transport in the bulk. Further on, Borghols et al. [45] suggested that the formation of the anatase Li_1TiO_2 phase at the particle surface during the lithium insertion is the limiting factor for the lithium ion transport since Li_1TiO_2 is characterized by poor ionic conductivity due to completely occupied interstitial octahedral sites. Whereas during the lithium extraction process the

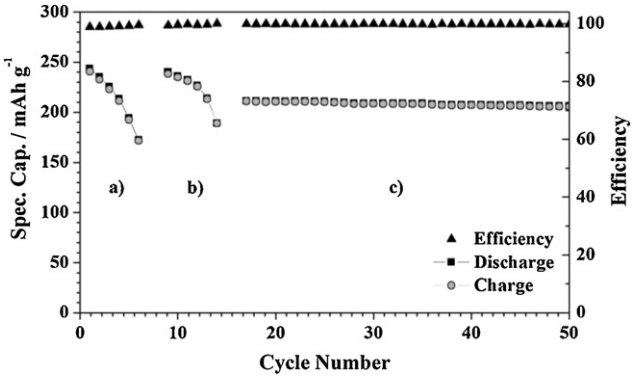

Fig. 10. Specific capacity of TiO_2-NR electrodes subjected to continuous galvanostatic charge discharge tests at different C rates. Lower cut-off potential: 1.2 V. (a) Increasing discharge rates (C/5, C/2, 1C, 2C, 5C, and 10C), constant charge rate: C/5. (b) Increasing charge rates (C/5, C/2, 1C, 2C, 5C, and 10C), constant discharge rate: C/5. (c) Constant charge and discharge rate: 1C. 1st cycle not shown.

surface Li_1TiO_2 phase is removed first (retransformation to phases with less lithium content), thereby enhancing the ionic conductivity and allowing easier transport of the lithium ions through the Li-poor(er) phase.

Finally, the excellent reversibility of lithium insertion/extraction into the investigated anatase TiO_2-NRs is demonstrated, by retrieving the former specific capacity for lower current densities and it should be pointed out that in a real battery, the achievable capacity at 10C discharge (charge for Li half cell) is 184 mAh g^{-1} (0.55 Li/TiO_2).

4. Conclusions

The lithium insertion/deinsertion processes in highly dispersed anatase TiO_2-NRs prepared by low-temperature synthesis were investigated. It has been demonstrated that the new composite preparation technique, which takes advantage of the OLEA capping, led to improved high rate performance and cycling stability of the synthesized NRs.

To the best of our knowledge, the TiO_2-NRs based electrodes presented in this manuscript showed the best results in terms of combined reversible capacity, long-term cycling performance, high power, and safety (operative potential window within the electrochemical stability window of common electrolytes). Hence, TiO_2-NRs appear as an appealing anode material candidate for the realization of safe, high performance, large electrochemical energy storage devices that are strongly required for the development of sustainable electric vehicles and effective use of renewable energies.

Acknowledgments

Financial support from the European Commission in the ORION project (229036) under the Seventh Framework Programme (7th FWP) is gratefully acknowledged.

The authors want to thank furthermore Dr. M. Lucia Curri and René Schmitz for performing TEM and Raman spectroscopy measurements, respectively.

References

[1] M.Z. Jacobson, M.A. Delucchi, Energy Policy 39 (2011) 1154–1169.
[2] M.A. Delucchi, M.Z. Jacobson, Energy Policy 39 (2011) 1170–1190.
[3] U. Eberle, M. Felderhoff, F. Schüth, Angewandte Chemie International Edition 48 (2009) 6608–6630.
[4] B.K. Sovacool, R.F. Hirsh, Energy Policy 37 (2009) 1095–1103.
[5] M. Armand, J.-M. Tarascon, Nature 451 (2008) 652–657.
[6] B. Scrosati, J. Garche, Journal of Power Sources 195 (2010) 2419–2430.
[7] A.S. Aricò, P. Bruce, B. Scrosati, J.M. Tarascon, W. van Schalkwijk, Nature Materials 4 (2005) 366–377.
[8] E. Peled, Journal of the Electrochemical Society 126 (1979) 2047–2051.
[9] R. Yazami, Electrochimica Acta 45 (1999) 87–97.
[10] S. Flandrois, B. Simon, CARBON: American Carbon Committee 37 (1999) 165–180.
[11] B. Zachau-Christiansen, K. West, T. Jacobsen, S. Atlung, Solid State Ionics 28–30 (1988) 1176–1182.
[12] L. Kavan, M. Grätzel, S.E. Gilbert, C. Klemenz, H.J. Scheel, Journal of the American Chemical Society 118 (1996) 6716–6723.
[13] T. Ohzuku, T. Kodama, T. Hirai, Journal of Power Sources 14 (1985) 153–166.
[14] S.-J. Bao, Q.-L. Bao, C.-M. Li, Zhi-Li Dong, Electrochemistry Communications 9 (2007) 1233–1238.
[15] J. Maier, Nature Materials 4 (2005) 805–815.
[16] M. Wagemaker, W.J.H. Borghols, F.M. Mulder, Journal of the American Chemical Society 129 (2007) 4323–4327.
[17] G. Sudant, E. Baudrin, D. Larcher, J.-M. Tarascon, Journal of Materials Chemistry 15 (2005) 1263–1269.
[18] C. Jiang, M. Wei, Z. Qi, T. Kudo, I. Honma, H. Zhou, Journal of Power Sources 166 (2007) 239–243.
[19] L. Kavan, J. Rathousky, M. Grätzel, V. Shklover, A. Zukal, The Journal of Physical Chemistry B 104 (2000) 12012–12020.
[20] J. Xu, C. Jia, B. Cao, W.F. Zhang, Electrochimica Acta 52 (2007) 8044–8047.
[21] X. Gao, H. Zhu, G. Pan, S. Ye, Y. Lan, F. Wu, D. Song, The Journal of Physical Chemistry B 108 (2004) 2868–2872.
[22] M. Pfanzelt, P. Kubiak, M. Wohlfahrt-Mehrens, Electrochemical and Solid State Letters 13 (2010) A91–A94.
[23] A.R. Armstrong, G. Armstrong, J. Canales, R. García, P.G. Bruce, Advanced Materials 17 (2005) 862–865.
[24] J. Li, Z. Tang, Z. Zhang, Electrochemical and Solid State Letters 8 (2005) A316–A319.
[25] M.G. Choi, Y.-G. Lee, S.-W. Song, K.M. Kim, Electrochimica Acta 55 (2010) 5975–5983.
[26] M. Wagemaker, A.P.M. Kentgens, F.M. Mulder, Nature 418 (2002) 397–399.
[27] M.L. Curri, R. Comparelli, P.D. Cozzoli, G. Mascolo, A. Agostiano, Materials Science and Engineering C 23 (2003) 285–289.
[28] G. Li, L. Li, J. Boerio-Goates, B.F. Woodfield, Journal of the American Chemical Society 127 (2005) 8659–8666.
[29] V. Subramanian, A. Karki, K.I. Gnanasekar, F.P. Eddy, B. Rambabu, Journal of Power Sources 159 (2006) 186–192.
[30] R. Buonsanti, V. Grillo, E. Carlino, C. Giannini, T. Kipp, R. Cingolani, P.D. Cozzoli, Journal of the American Chemical Society 130 (2008) 11223–11233.
[31] M.R. Ranade, A. Navrotsky, H.Z. Zhang, J.F. Banfield, S.H. Elder, A. Zaban, P.H. Borse, S.K. Kulkarni, G.S. Doran, H.J. Whitfield, Proceedings of the National Academy of Sciences of the United States of America 99 (2002) 6476–6481.
[32] A.A. Levchenko, G. Li, J. Boerio-Goates, B.F. Woodfield, A. Navrotsky, Chemistry of Materials 18 (2006) 6324–6332.
[33] Y. Chen, K.S. Kang, K.H. Yoo, N. Jyoti, J. Kim, The Journal of Physical Chemistry C 113 (2009) 19753–19755.
[34] D.J. Reidy, J.D. Holmes, M.A. Morris, Journal of the European Ceramic Society 26 (2006) 1527–1534.
[35] T. Tong, J. Zhang, B. Tian, F. Chen, D. He, Materials Letters 62 (2008) 2970–2972.
[36] J. De Gelder, K. De Gussem, P. Vandenabeele, L. Moens, Journal of Raman Spectroscopy 38 (2007) 1133–1147.
[37] D.S. Knight, W.B. White, Journal of Materials Research 4 (1989) 385–393.
[38] R. Baddour-Hadjean, J.-P. Pereira-Ramos, Chemical Reviews 110 (2010) 1278–1319.
[39] R. Baddour-Hadjean, S. Bach, M. Smirnov, J.-P. Pereira-Ramos, Journal of Raman Spectroscopy 35 (2004) 577–585.
[40] K. Woan, G. Pyrgiotakis, W. Sigmund, Advanced Materials 21 (2009) 2233–2239.
[41] A. Heller, Accounts of Chemical Research 28 (1995) 503–508.
[42] O.-O. Prieto-Mahaney, N. Murakami, R. Abe, B. Ohtani, Chemistry Letters 38 (2009) 238–239.
[43] M. Wagemaker, R. van de Krol, A.P.M. Kentgens, A.A. van Well, F.M. Mulder, Journal of the American Chemical Society 123 (2001) 11454–11461.
[44] R.J. Cava, D.W. Murphy, S. Zahurak, A. Santoro, R.S. Roth, Journal of Solid State Chemistry 53 (1984) 64–75.
[45] W.J.H. Borghols, D. Lutzenkirchen-Hecht, U. Haake, E.R.H. van Eck, F.M. Mulder, M. Wagemaker, Physical Chemistry Chemical Physics 11 (2009) 5742–5748.
[46] R. van de Krol, A. Goossens, J. Schoonman, The Journal of Physical Chemistry B 103 (1999) 7151–7159.
[47] M. Song, X. Feng, X. Lu, X. Wang, Electroanalysis 22 (2010) 668–672.
[48] D. Chu, Y. Hou, J. He, M. Xu, Y. Wang, S. Wang, J. Wang, L. Zha, Journal of Nanoparticle Research 11 (2009) 1805–1809.
[49] U. Lafont, D. Carta, G. Mountjoy, A.V. Chadwick, E.M. Kelder, The Journal of Physical Chemistry C 114 (2010) 1372–1378.
[50] M. Fittipaldi, M.L. Curri, R. Comparelli, M. Striccoli, A. Agostiano, N. Grassi, C. Sangregorio, D. Gatteschi, The Journal of Physical Chemistry C 113 (2009) 6221–6226.
[51] C. Sciancalepore, A. Agostiano, T. Cassano, A. Valentini, M.L. Curri, M. Striccoli, D. Mecerreyes, R. Tommasi, Nanotechnology (2008) 19.
[52] P.D. Cozzoli, A. Kornowski, H. Weller, Journal of the American Chemical Society 125 (2003) 14539–14548.
[53] T.J. Trentler, T.E. Denler, J.F. Bertone, A. Agrawal, V.L. Colvin, Journal of the American Chemical Society 121 (1999) 1613–1614.